Detection of the compressed primary stellar wind in η Carinae[*]

M. Teodoro[1,2]

T. I. Madura[1,3]

T. R. Gull[1]

M. Corcoran[4,5]

K. Hamaguchi[4,6]

[1]Astrophysics Science Division, Code 667, NASA Goddard Space Flight Center, Greenbelt, MD 20771, USA

[2]CNPq/Science without Borders Fellow.

[3]NASA Postdoctoral Program Fellow.

[4]CRESST and Xray Astrophysics Laboratory, Code 662, NASA Goddard Space Flight Center, Greenbelt, MD 20771, USA

[5]Universities Space Research Association, 10211 Wincopin Circle, Suite 500 Columbia, MD 21044, USA

[6]Department of Physics, University of Maryland, Baltimore County, 1000 Hilltop Circle, Baltimore, MD 21250, USA.

mairan.teodoro@nasa.gov

ABSTRACT

A series of three *HST/STIS* spectroscopic mappings, spaced approximately one year apart, reveal three partial arcs in [Fe II] and [Ni II] emissions moving outward from η Carinae. We identify these arcs with the shell-like structures, seen in the 3D hydrodynamical simulations, formed by compression of the primary wind by the secondary wind during periastron passages.

Subject headings: Stars: individual (η Carinae) — stars: massive — binaries: general

1.   Introduction

η Carinae (hereafter η Car) is now recognized to be a massive binary system in a highly eccentric orbit ($e > 0.9$). The primary star, η Car A, is in the luminous blue variable (LBV) phase, with a luminosity of $10^{6.7}$ $L_\odot$ and mass of about 120 $M_\odot$ (Davidson & Humphreys 1997). It is surrounded by a massive stellar wind ($\dot{M} \sim 10^{-3}$ $M_\odot\,yr^{-1}$, $v_\infty \approx 420$ km s^{-1}; Groh et al. 2012) that interacts with a companion, η Car B, that has not been detected directly yet. The physical parameters of η Car B are, thus, inferred from X-ray ($\dot{M} \sim 10^{-5}$ $M_\odot\,yr^{-1}$, $v_\infty \approx 3000$ km s^{-1}; Pittard & Corcoran 2002) and photoionization modeling ($\sim 10^5$ $L_\odot$, 34000 K$< T_{\rm eff} < 3900$ K; Verner et al. 2005; Teodoro et al. 2008; Mehner et al. 2010).

The orbital orientation is such that the orbital plane has an inclination of $i \approx 140°$, with the semi-major axis pointing along position angle (P. A.[1]) 314° and longitude of periastron $\omega \approx 240°$ (Gull et al. 2009, 2011; Madura et al. 2012). In this configuration, η Car B is in front of η Car A at apastron, and the orbital angular momentum vector is parallel to the symmetry axis of the bipolar Homunculus nebula that surrounds the system.

Projected on the sky, the secondary star directly illuminates and photo-ionizes the circumstellar material within 1200 AU of the binary system primarily to the northwest, where the material is primarily approaching the observer. The companion star spends most of the orbit near apastron, so that the undisturbed wind from η Car A is located on the far side of the system, red-shifted as seen from Earth, and largely unaffected by the ionizing radiation from η Car B.

During periastron passage, η Car B approaches within 1-2 AU of η Car A, leading to rapid changes in the shape of the wind-wind interaction surface and confinement of the

---

[1]P. A. is defined as the angle, in the plane of the sky, eastward of North.

far-UV flux from η Car B. Hydrodynamical simulations (Madura et al. 2012, T. Madura et al. 2013, in preparation) show that, after each periastron passage, a highly-distorted volume of hot, low density secondary wind pushes outward into the slow, high-density primary wind, leading to the formation of a thin, high density wall surrounding the lower density, trapped wind of η Car B. This dense wall is accelerated to velocities somewhat higher than the terminal velocity of η Car A and expands both in the orbital plane and perpendicular to it, creating a thin, high-density sheet of trapped primary wind material.

Using spectral imaging maps from the Space Telescope Imaging Spectrograph (*STIS*), on board the Hubble Space Telescope (*HST*), we identify structures which are consistent with these walls of compressed primary wind material. We identify three partial arcs formed by the close passage of η Car B around the primary star over the last 3 orbital cycles, and using the *STIS* maps, we determine their space velocity and age.

2. Observations, data reduction, and analysis

Observations using *HST/STIS* were accomplished through three guest observer programs, 12013 (2010 October 26), 12508 (2011 November 20), and 12750 (2012 October 18), using the G430M and G750M gratings, centered at 4706Å and 7283Å, respectively, in combination with the $52'' \times 1''$ aperture. An extended region, covering $1''$ to $2'' \times 6.4''$, centered upon η Car, was mapped using $0.05''$ spacing offsets at P. A. constrained by the spacecraft. Exposures were approximately 30 seconds using CRSPLIT=2. An additional 7 position sub-map, also centered on η Car, employed shorter exposures to allow for potential saturation of continuum on the central positions.

Data were reduced with *STIS* GTO IDL-based[2] tools similar to the standard pipeline

---

[2]IDL is a trademark of Exelis Visual Information Solutions, Inc.

reduction tools (Bostroem & Proffitt 2011), but with improved ability to spatially align the spectra to sub-pixel accuracy. For each emission line of interest, continuum levels were fitted for each spatial position along the aperture and a re-sampled data cube was generated, with the coordinates of right ascension and declination at $0.05''$ spacing, and Doppler velocity at $20\,\mathrm{km\,s^{-1}}$ intervals.

Since we are interested in structures formed in the primarywind around periastron, here we focus only on the following low-ionization lines: [Fe II] ($\lambda_0 = 4729.39$, 4776.05, 4815.88, 7157.13)[3] and [Ni II] ($\lambda_0 = 7413.65$). Observations from program 12013 (2010 October 26) did not include maps of [Fe II] $\lambda7157.13$ and [Ni II] $\lambda7413.65$.

Visual examination of iso-velocity images in each data cube revealed multiple arcs in the low-ionization spectral lines used in this work. Sample images are presented in Figure 1 for the [Fe II] $\lambda4815$ transition. These arcs are visible between P. A. 90° and 200°. We identified at least three sets of partial arcs, labelled A1, A2, and A3 in Figure 2. The two innermost arcs, A1 and A2, are conspicuously detected in all of the transitions from [Fe II] and [Ni II]. The outermost arc, A3, is very faint.

These arcs are not artifacts of the HST/STIS point spread function (PSF). The *HST/STIS* PSF diffractive rings vary slowly with wavelength, are symmetric about the central core and have amplitudes substantially weaker than the partial rings apparent in the images (Krist et al. 2011). As shown in the discussion below, these features correlate with multiple forbidden line structures seen at different wavelengths, expanding away from the central source.

Comparison of the same iso-velocity image for different epochs (2010 October 26, 2011 November 20, and 2012 October 18) revealed that A1, A2, and A3 move outward from the

---

[3]All rest wavelengths, λ_0, are in Å, in vacuum (Zethson et al. 2012).

central source (Figure 3). Because A3 is faint and hard to see in all the images, and A1 is affected by uncertainties in the continuum subtraction method close to the central source, we concentrate our analysis on A2. We note, however, that all three arcs seem to expand at approximately the same rate, but some extended parts become very distorted or diluted, which makes the determination of accurate positions a difficult task.

The position of the eastern portion of A2, relative to the central source, was measured using a radial flux profile cut along its direction (Figure 3). For each dataset (2010, 2011, and 2012), we extracted the flux profile between $0'' < r < 0.9''$ and $100° < \mathrm{P.\,A.} < 105°$, where the emission from A2 is strongest.

We used three different methods for measuring the peak position in the radial flux profile curve. The first is a simple gaussian model, which is a good approximation when the flux profile of the shell is somewhat symmetric. The second method relies on the barycenter of the flux profile, and the third, developed by Blais & Rioux (1986), is based on the analysis of the derivative of the observed profile. The position of the peak is the median value of these methods.

A comprehensive study comparing several methods to determine peak positions with sub-pixel accuracy, including the three methods used here, was done by Fisher & Naidu (1996). The reader is referred to that paper for further details. Based upon the individual measurement errors, we estimate an accuracy of 0.25 pixel ($0.013''$) for the position of the shell using the median value of the three methods mentioned before. The total error, however, may be larger than that because it is dominated by the dispersion in the measured position for various forbidden lines.

3. Results

We note that A2 is moving outwards with a proper motion $\mu = (0.05 \pm 0.01)'' \, \text{yr}^{-1}$, on the plane of the sky (Figure 4), a value suspiciously close to the pixel size. However, many other regions across the field of view are fixed in position from image to image, giving us confidence that the images are all spatially registered correctly. Furthermore, the motion of portions of A2 depends on the local Doppler velocity (*cf.* Figure 4). Hence, the detected motion is not caused by a systematic misalignment of the images.

The projected radius (r_{p}), at a given Doppler velocity (V_{D}), of a shell moving with space velocity V, during a time t, is given by

$$r_{\text{p}}(t) = V \, t \, \sin\left(\arccos\left(\frac{V_{\text{D}}}{V}\right)\right). \tag{1}$$

Taking the difference of the projected radius of A2, at two epochs separated by a time interval $\Delta t = t_2 - t_1$, leads to

$$r_{\text{p}}(t_2) - r_{\text{p}}(t_1) = V \, \Delta t \, \sin\left(\arccos\left(\frac{V_{\text{D}}}{V}\right)\right). \tag{2}$$

Setting the observations made in 2010 Oct. 26 as baseline, we have $\Delta t = 1.07$ and 1.98 yr, for the two subsequent datasets. Thus, we used the measured projected position for A2 in the range $-40 \leq V_D \leq +40 \, \text{km s}^{-1}$ (this is the small angle regime, where $V_D/V \ll 1$) to estimate the space velocity, which resulted in $V = (475 \pm 29) \, \text{km s}^{-1}$. The age of A2, $t(\text{A2})$, in 2010, is thus obtained from $< r_{\text{p}}(\text{A2}) > /V = (9.65 \pm 0.55)$ yr, where $< r_{\text{p}}(\text{A2}) >= 0.41''$ is the average projected distance of A2, relative to the central source, at that epoch.

Assuming that A1 and A3 are moving at the same constant space velocity as A2, then, for a given epoch, we have

$$\frac{r_{\text{p}}(\text{A1})}{r_{\text{p}}(\text{A2})} = \frac{t(\text{A1})}{t(\text{A2})}, \tag{3}$$

where $r_\mathrm{p}(\mathrm{A}1)$ is the average projected distance of A1 from the central source, and $t(\mathrm{A}1)$ is its age. In 2010 and 2011, A1 was too close to the central source. Thus, we used the observations of 2012 to measure the position and then estimate the age. In 2012, we have $r_\mathrm{p}(\mathrm{A}1) \approx 0.22''$, resulting in $t(\mathrm{A}1) = (5.98 \pm 0.92)$ yr. The relation described in equation (3) also applies to A3, resulting in $t(\mathrm{A}3) = (17.13 \pm 0.95)$ yr, since it was observed at $r_\mathrm{p}(\mathrm{A}3) \approx 0.6''$ in 2012. The rather large errors are dominated by uncertainties in the position due to the proximity to the central source for A1, and the weak emission of A3.

Correcting for the time interval between the 2012 and 2010 observations, and comparing the ages in 2012, we finally have $t(\mathrm{A}1) = 5.98$, $t(\mathrm{A}2) = 11.63$, and $t(\mathrm{A}3) = 17.13$ yr. This means that each shell is created approximately 5.6 yr after the earlier one, showing that they are directly tied to the orbital period of the binary system ($P = 5.54$ yr; Damineli et al. 2008).

To test for the consistency of our results across the range of Doppler velocities where A2 is observed, we adopted two simplified models in which we consider A2 to be a shell with either a spherical or an ellipsoidal geometry centered on η Car, and allowed it to expand, at a constant space velocity of 475 $\mathrm{km\,s^{-1}}$, during the corresponding age of A2 at each epoch of observations ($t1_\mathrm{exp}$, $t2_\mathrm{exp}$, and $t3_\mathrm{exp}$ in Figure 4).

At line of sight velocities near zero, both the spherical and the ellipsoidal models reproduce the observations very well, with standard deviations $< 0.015''$. However, the spherical model does not match the observed position of A2 at red-shifted velocities (> 100 $\mathrm{km\,s^{-1}}$); A2 moves slower than predicted. We then considered the ellipsoidal model, to which we added some degree of asymmetry by changing the geometrical parameters (*i.e.*, semi-major axis, eccentricity, orientation etc), improving the quality of the matching by a factor of 41% over the spherical model, for the full range of Doppler velocities. The final standard deviation for the ellipsoidal and spherical models is $0.034''$ and $0.048''$, respectively.

The ellipsoidal model better matches the observed positions because we can use two independent components for the space velocity: one along the ellipsoid's major axis (fixed at 483 km s^{-1}) and another along the minor one (300 km s^{-1}). It is important to remark that this is *only* a parametrization to reproduce the observed pattern of the Doppler velocity and *is not* a physical model of the geometry of A2. In our ellipsoidal model, when the angle of rotation (θ) is zero[4], the major axis is aligned in the plane of the sky; the minor is in the line of sight. We set the third axis to be the same size as the projection of the major axis onto the plane of the sky, the combination of which produces a circle projected on the sky. Therefore, our results suggest that A2 does not expand isotropically, *i.e.*, with the same space velocity in all directions.

4. Discussion and Conclusions

We used the critical density for each forbidden line, calculated using the CHIANTI atomic database, to infer the typical local densities of the arcs. The outermost arc, A3, seen in the [Ni II] transitions but weakly in the [Fe II], must have a density in the range $0.8 - 4 \times 10^6$ cm^{-3}. The strong [Fe II] emission from A1 and A2, indicates that their densities must be $> 4 \times 10^6$ cm^{-3}.

Assuming that A2 is half a spherical shell (*cf.* Figure 5) with average radius of $0.4''$ (projected distance from the central source, at zero Doppler velocity, in 2010) and thickness of $0.05''$ (must be less than this since we cannot spatially resolve the shells), and using the critical density calculated before, we estimate a total mass of 2.6×10^{-3} M$_\odot$, for solar metallicity.

Models for the primary star predict that its wind density should drop below 10^6 cm^{-3}

---

[4]The best overall match for the ellipsoidal model occurred for $\theta = 8°$.

for projected distances greater than $0.2''$ (Hillier et al. 2001; Groh et al. 2012). Since we detected arcs exceeding 10^6 cm^{-3} out to $0.6''$, this is naturally explained by the primary wind being compressed – a factor of 30 – by the secondary wind during periastron passage. This is also supported by the fact that the average age difference between the arcs is approximately 5.6 yr, nicely matching the binary system's period.

The primary mass-loss rate required to produce a shell with the same mass and geometry as A2, over a time interval equal to the binary's period, is 9.3×10^{-4} M$_\odot$ yr^{-1}, in agreement with the latest results from 2D radiative transfer spectral modeling $(8.5 \times 10^{-4}$ M$_\odot$ yr^{-1}; Groh et al. 2012). We note, however, that our result must not be taken as a strict lower or upper limit, since the actual geometry and thickness of A2 may be different from what we assumed.

Simulations using 3D smoothed particle hydrodynamics (3D SPH) reveal compressed regions of the primary wind formed during the periastron passages and maintained for multiple cycles by the hot, low density, residual secondary wind (Figure 5). These simulations predict that these compressed regions accelerate from the primary wind terminal velocity $(v_\infty = 420$ km s^{-1}; Groh et al. 2012) to about $460 - 470$ km s^{-1} (T. Madura et al. 2013, in prep.), which is consistent with our derived expansion velocity of 475 km s^{-1} for the shells.

The departure from spherical symmetry for high red-shifted Doppler velocities suggests that the shells do not expand with the same velocity in all directions. This is explained by the fact that 3D SPH simulations show that material located in the orbital plane moves faster than material located off the plane. Thus, the observed Doppler velocity is a combination of velocities from different emitting regions along a specific viewing angle, which, in turn, depends upon the orientation of the shells on the sky, ultimately defined by the orbital orientation.

During periastron passages, SPH 3D simulations show that the secondary star creates a cavity deep within the primary wind, pushing a shell outwards. Since the low density secondary wind is moving at ≈ 3000 km s^{-1}, the interaction with the high density, relatively slow primary wind results in the formation of a high density, thin shell accelerated to velocities slightly higher than the terminal velocity of the primary wind. Hence, the geometry of the shell is strongly affected by the physical parameters of the binary system, and the projected appearance on the sky is defined by the inclination of the orbital plane.

The latitudinal extent of the shells is controlled by the asymptotic opening angle, θ_∞, of the wind-wind collision region, given by (Usov 1992)

$$\theta_\infty = \frac{2\pi}{3}\left(1 - \frac{\eta^{2/5}}{4}\right)\eta^{1/3} \tag{4}$$

where $\eta = \dot{M}_B\, v_{\infty B}/\dot{M}_A\, v_{\infty A}$ is the ratio of the secondary to the primary wind momentum, $\dot{M}$ and v_∞ are the mass-loss rate and terminal velocity of the wind, and the subscript A and B refer to the primary and secondary star, respectively.

Assuming fixed parameters for the secondary wind, a large primary mass loss rate decreases the bow shock opening angle θ_∞, so that the compressed primarys wind material is trapped near the orbital plane (Figure 5(c)); a low mass-loss rate increases θ_∞, and the compressed primary wind can extend well off the orbital plane (Figure 5(d)). This means that the geometry of the circumstellar arcs is an excellent diagnostic of the primary mass-loss rate: a lower mass loss rates produces a nearly continuous arc seen in projection around the star, while a higher mass loss rate produces a shorter, broken arc.

The existence of a discontinuity in the arcs that we observe, more pronounced in A1 as a lack of emission at P. A.$\approx 135°$, yields a lower limit to the mass-loss rate of the primary star. SPH simulations in 3D show that such broken rings are only apparent if the primary mass-loss rate is above 2.5×10^{-4} M$_\odot$ yr^{-1}, which suggests that, at least for the last event, the primary mass-loss rate must have exceeded this value.

Our results also constraint the orbital orientation, with periastron occuring between $200° < \omega < 270°$, *i.e.*, during periastron, the primary star is between the observer and the secondary star. The opposite configuration, where the secondary, at periastron, is between the observer and the primary star, would produce blue-shifted shells seen to the northwest of the central source, rather than the red-shifted features to the southeast that we observe.

Finally, we note that our results assume a constant shell space velocity. If these shells were accelerated at any time since their formation, their age, as derived here, would be overestimated, *i.e.*, the shells would be younger than estimated, but the difference between the ages would remain the same 5.6 yr derived in this paper.

Facilities: HST (STIS).

REFERENCES

Blais, F., & Rioux, M. 1986, Signal Processing, 11, 145

Bostroem, K. A., & Proffitt, C. 2011, STIS Data Handbook, HST Data Handbooks, -1

Damineli, A., Hillier, D. J., Corcoran, M. F., et al. 2008, Astronomical Journal, 384, 1649

Davidson, K., & Humphreys, R. M. 1997, Annual Review of Astron and Astrophys, 35, 1

Fisher, R. B., & Naidu, D. K. 1996, in link.springer.com (Berlin, Heidelberg: Springer Berlin Heidelberg), 385–404

Groh, J. H., Hillier, D. J., Madura, T. I., & Weigelt, G. 2012, Astronomical Journal, 423, 1623

Gull, T. R., Madura, T. I., Groh, J. H., & Corcoran, M. F. 2011, Publications of the Astron. Soc. of Australia, 743, L3

Gull, T. R., Nielsen, K. E., Corcoran, M. F., et al. 2009, Monthly Notices of the RAS, 396, 1308

Hillier, D. J., Davidson, K., Ishibashi, K., & Gull, T. 2001, Astrophysical Journal, 553, 837

Krist, J. E., Hook, R. N., & Stoehr, F. 2011, in SPIE Optical Engineering + Applications, ed. M. A. Kahan (SPIE), 81270J–81270J–16

Madura, T. I., Gull, T. R., Owocki, S. P., et al. 2012, Astronomical Journal, 420, 2064

Mehner, A., Davidson, K., Ferland, G. J., & Humphreys, R. M. 2010, Astronomical Journal, 710, 729

Pittard, J. M., & Corcoran, M. F. 2002, Astronomy and Astrophysics, 383, 636

Smith, N. 2006, Astrophysical Journal, 644, 1151

Teodoro, M., Damineli, A., Sharp, R. G., Groh, J. H., & Barbosa, C. L. 2008, Astronomical Journal, 387, 564

Usov, V. V. 1992, Astronomical Journal, 389, 635

Verner, E., Bruhweiler, F., & Gull, T. 2005, Astrophysical Journal, 624, 973

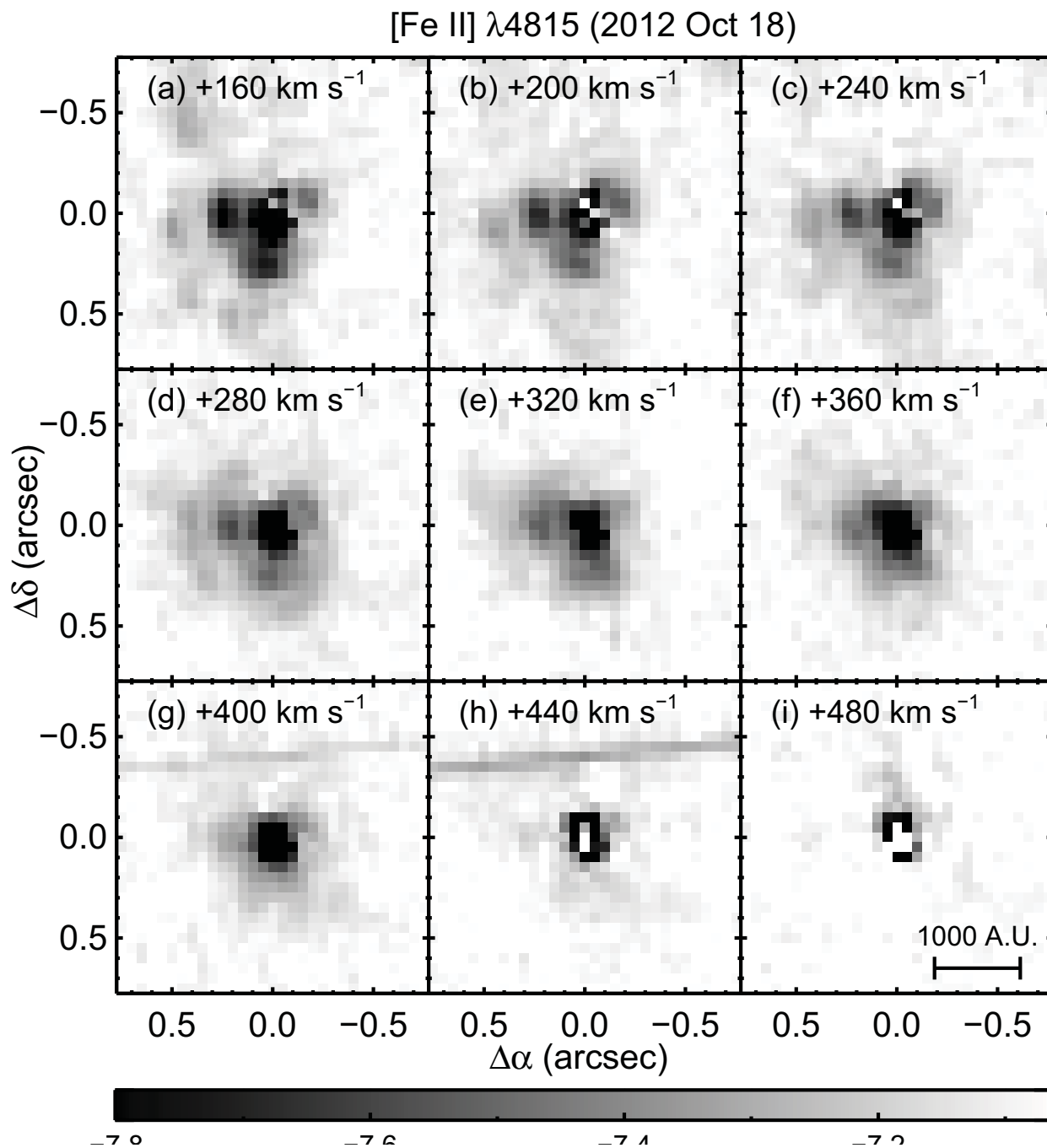Zethson, T., Johansson, S., Hartman, H., & Gull, T. R. 2012, Astronomy and Astrophysics, 540, A133

Fig. 1.— Iso-velocity images of [Fe II] $\lambda4815$ for the observations of 2012 October 18. The velocities are indicated in each panel. The linear structures that appear in panels (g) and (h) are the result of a bad CCD column. The physical scale is based on an adopted distance of 2350 pc (Smith 2006). We note that there are no extended structures at Doppler velocities higher than $+440$ km s^{-1}.
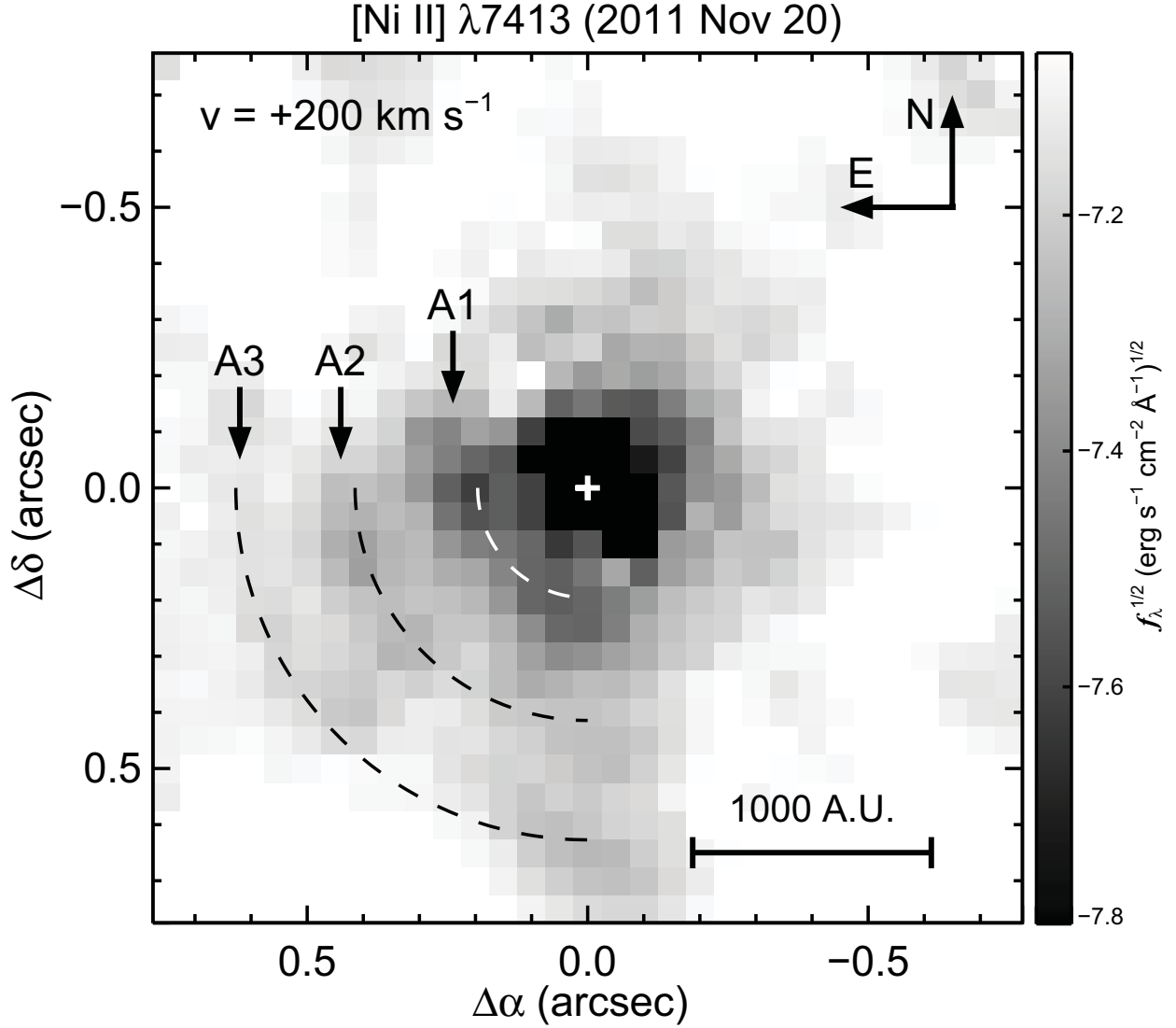
Fig. 2.— Iso-velocity image of [Ni II] $\lambda 7413$ at $+200$ km s^{-1}, obtained in 2011 November 20. The arcs discussed in this work are indicated by the arrows and were labeled A1, A2, and A3. The dashed lines show the expected position of three spherical shells traveling at a constant speed of 475 km s^{-1} for 4.5, 10, and 15.5 years, for the inner, middle, and outer arcs, respectively. To determine the expansion rate, we restricted our measurements to the eastern component of A2.
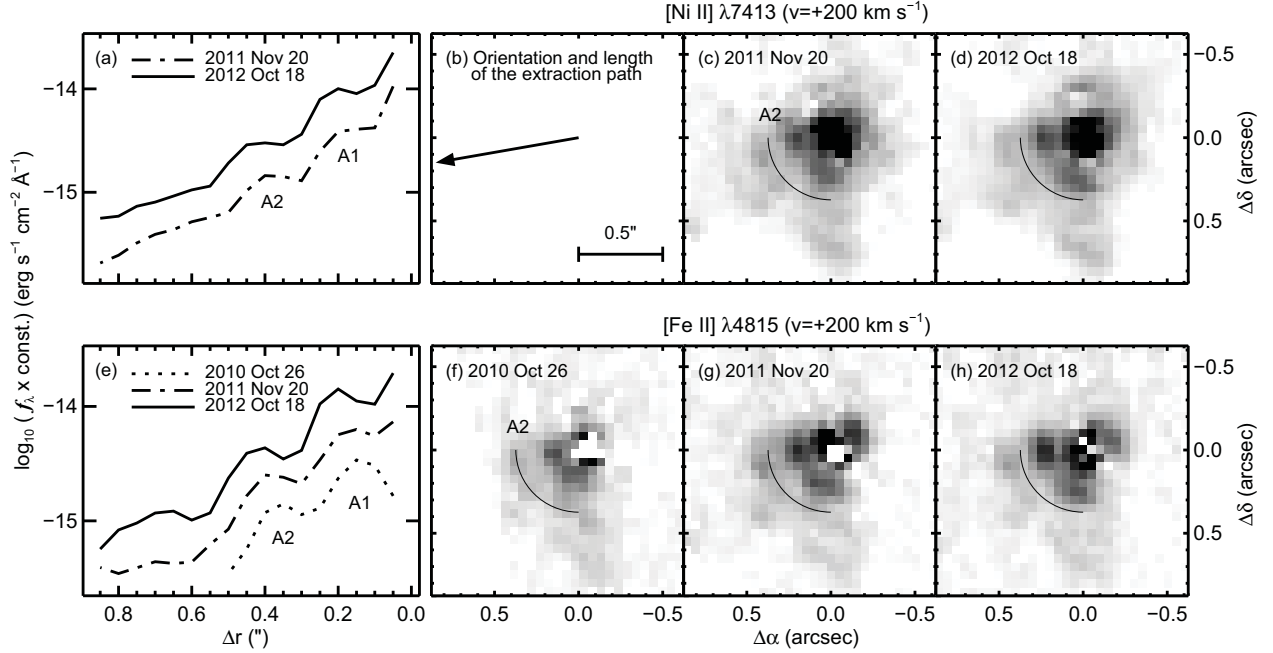
Fig. 3.— Flux profiles and iso-velocity images of two forbidden lines: (*a*) and (*e*) are for [Ni II] $\lambda 7413$ and [Fe II] $\lambda 4815$, respectively, along the position indicated by the arrow in panel (*b*), which has a length of approximately $0.9''$ and P. A. $= 100°$. The flux profiles were extracted from the iso-velocity images on the right. To illustrate the detected outward motion, in panels (*c*), (*d*), (*f*), (*g*), and (*h*) the curved solid line marks the position of A2 in 2010 October 26. For better visualization, the flux profiles were shifted in the vertical direction.
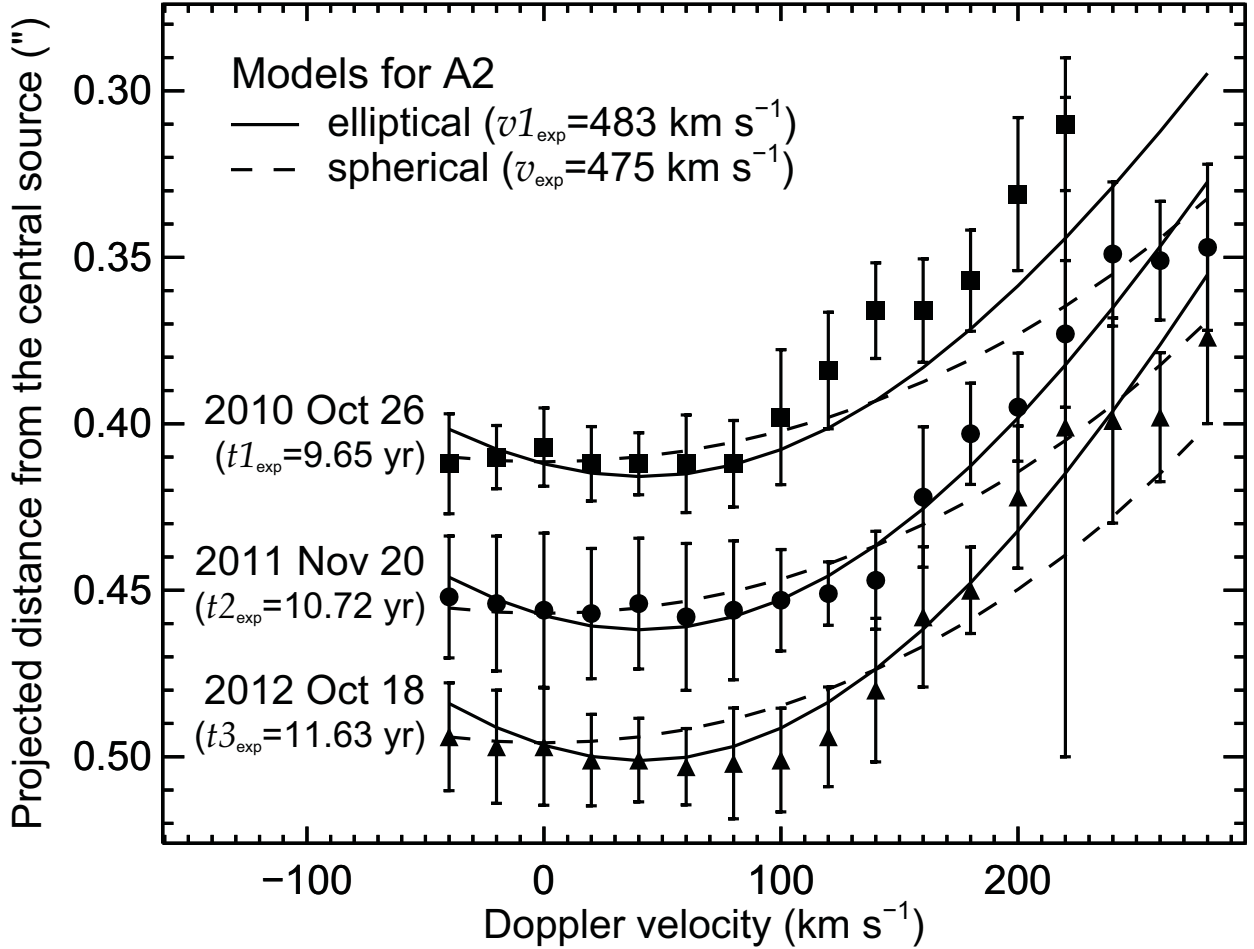
Fig. 4.— Observed position of A2 as a function of Doppler velocity for the indicated epochs. Dashed lines show the projected position expected for a spherical shell expanding at 475 km s^{-1} during $t1_{\mathrm{exp}}$, $t2_{\mathrm{exp}}$, and $t3_{\mathrm{exp}}$. The solid lines show the same, but for an ellipsoidal shell with space velocity of 483 km s^{-1} along the major axis, which is 8° off the plane of the sky, away from the observer. At zero Doppler velocity, both models have the same projected size on the sky.
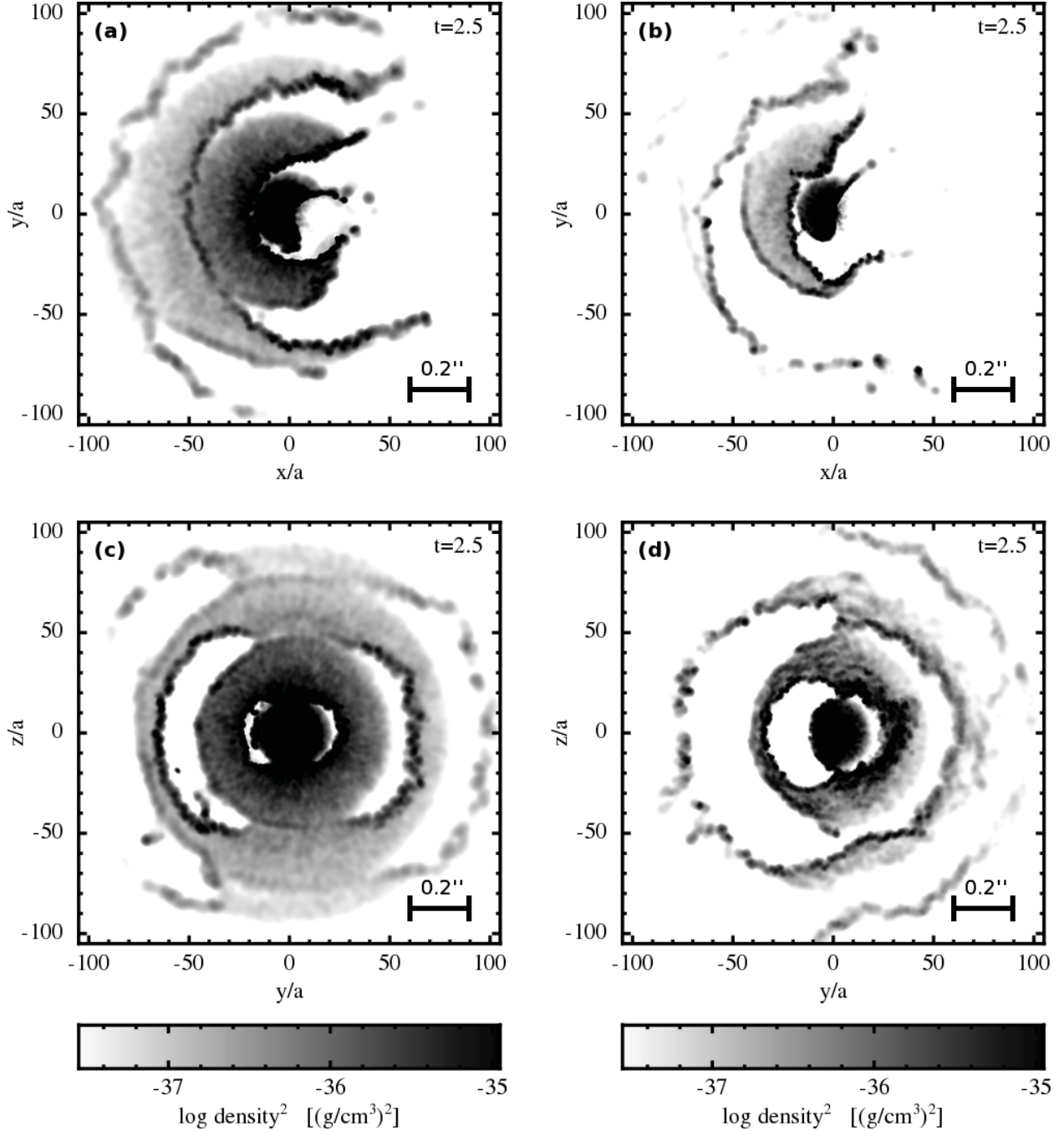
Fig. 5.— 3D SPH simulations showing the formation and geometry of high density regions due to the compression of the primary wind by the secondary wind, in two different regimes for the primary mass-loss rate: 8.5×10^{-4} M$_\odot$ yr^{-1} (left) and 2.5×10^{-4} M$_\odot$ yr^{-1} (right). *Upper panels*: slices in the orbital plane (xy). *Lower panels*: slices perpendicular to the orbital plane (yz). In the high mass-loss rate regime, there is a gap in the polar region that is not observed in the lower mass-loss rate regime. The lower and upper limits of the density scale correspond to the critical density values for [Ni II] and [Fe II], respectively.